Radar Interferogram Filtering for Geophysical Applications

Richard M. Goldstein and Charles L. Werner

Jet Propulsion Laboratory, Pasadena, California

Abstract. Synthetic aperture radar interferometry has wide application in the measurement of geophysical quantities such as crustal deformation, glacier motion, and surface topography. Use of interferometry is often impeded by decorrelation from thermal noise, temporal change, and the baseline geometry. Power spectra of interferograms are typically the sum of a single narrow-band component combined with broad-band noise. We describe a new adaptive filtering algorithm that dramatically lowers phase noise, improving both measurement accuracy and phase unwrapping, while demonstrating graceful degradation in regions of pure noise. Interferometric data from the Jakobshavns Isbræ glacier is used to demonstrates the filter performance.

1. Introduction

Synthetic aperture radar (SAR) interferometry has been proven to be a powerful technique for measurement of the earth surface. Applications range from the generation of high resolution topographic maps [Li and Goldstein 1990; Zebker et al. 1992] to measurement of flow in glaciers and ice sheets [Goldstein et al. 1993; Joughin et al. 1996] and surface displacements associated with crustal deformation [Massonnet et al. 1993; Peltzer and Rosen 1995; Rosen et al. 1996].

Acquisition of the interferometric data requires two or more SAR imaging passes of the area under study. The basic data acquisition geometry is shown in Figure 1. Interferometric measurements may be separated in space and or time depending on the specific application or system. Studies of processes that evolve in time, such as glacial flow or tectonic plate motion require data acquired at two different times in order to detect the motion that occurs during the interval. Conversely, the optimum strategy for topographic mapping requires simultaneous acquisition of the images forming the interferometric pair, thereby avoiding temporal decorrelation in the scene and the phase distortions arising from ionospheric and tropospheric turbulence [Goldstein 1995].

Differential interferometry measures changes in line-of-sight distance that occurs during the time interval

Figure 1

between SAR data acquisitions. The line of sight sensitivity to surface displacement δ_r, given a phase measurement error $d\phi$ is

$$\delta_r = -\frac{\lambda}{4\pi}d\phi \, , \qquad (1)$$

where λ is the radar wavelength.

Topographic mapping uses the interferometric phase to measure the difference in the length of the look vectors from points separated by the baseline B. The standard deviation of the height σ_h is a function of the slant range ρ, baseline geometry, look angle θ, and is linearly proportional to standard deviation of the phase σ_ϕ:

$$\sigma_h = \frac{\lambda}{4\pi}\frac{\rho \sin\theta}{B\cos(\theta - \alpha)}\sigma_\phi \, . \qquad (2)$$

Sources of phase noise include decorrelation due to the baseline separation and surface slope, thermal noise, scene rotation, and temporal change [Zebker and Villasenor 1992]. For differential interferometric applications, the temporal decorrelation introduced by random shifts of the scattering elements or changes in dielectric constant is the most serious limitation to the general application of the technique on a global basis. The complex correlation coefficient γ of the interferometric data is defined by

$$\gamma = \frac{< E_1 E_2^* >}{\sqrt{< |E_1|^2 >< |E_2|^2 >}} \qquad (3)$$

with E_1 and E_2 the complex echo amplitudes received at the two antenna locations and the brackets represent an ensemble average. In practice, a finite number of independent "looks" are averaged in order to estimate the correlation. The interferometric phase ϕ is the argument of γ while the correlation magnitude ranges between 0 and 1. The measure of γ can be related to δ_r or σ_h through computation of the phase standard deviation σ_ϕ as a function of correlation. A Monte Carlo simulation of the σ_ϕ as a function of γ and number of independent looks is shown in Figure 2.

Figure 2

2. Interferogram Filtering Algorithm

The interferogram power spectrum is characterized by a narrow band component, from surface backscatter and a broadband noise component. In the absence of multiple scattering in regions of layover, only a single local fringe frequency is present. The local interferometric phase slope with respect to slant range ρ as a function of surface slope angle ξ is given by

$$\frac{d\phi}{d\rho} = \frac{4\pi}{\lambda}\frac{B_\perp \delta_r}{\rho \tan(\theta - \xi)} \, . \qquad (4)$$

The non-stationarity of the fringe spectrum requires an adaptive algorithm that matches the local fringe spectrum and this is the basis of the filter algorithm.

The interferogram $I(x, y)$ is segmented into overlapping square patches and a two-dimensional FFT $\tilde{I}(u, v)$ is evaluated and then detected to yield the local power spectrum $S(u, v)$,

$$S(u, v) = |\,\text{FFT}\,\{I(x, y)\}\,| \ . \tag{5}$$

The power spectrum $S(u, v)$ is convolved with a rectangular smoothing window $W(u, v)$ (nominally 3×3) to reduce the variance of the estimate,

$$\hat{S}(u, v) = S(u, v) \otimes W(u, v) \ . \tag{6}$$

The adaptive filter $Z(u, v)$ is derived from the power spectrum by the non-linear operation

$$Z(u, v) = \left[\hat{S}(u, v) \right]^{\alpha} \ , \tag{7}$$

where the exponent α typically lies in the range of $[0, 1]$. The frequency domain filter Z is then used to multiply the Fourier transform of the interferogram patch. An inverse transform is then applied to recover the filtered interferogram samples $\hat{I}(x, y)$,

$$\hat{I}(x, y) = \text{FFT}^{-1} \left\{ \tilde{I}(u, v)\, Z(u, v) \right\} \ . \tag{8}$$

For the case $\alpha = 0$, no filtering occurs, while for $\alpha = 1$ the filtering is strong. Useful values of α lie in the range .2 to .5 given interferograms with moderate correlation $\gamma > .25$. Interferograms with very low correlation benefit from larger patch sizes and higher values of α. Patches are overlapped to attenuate discontinuities at the boundaries. Overlap is selected to be 75% in both the along-track and cross-track directions with a triangular weighting in x and y. The effect of this window is to obtain the sum of weighted contributions from each of the patches that cover a particular interferogram sample.

To observe the filter bandwidth characteristics consider a Gaussian shaped power spectrum of the form

$$S(u, v) = \exp \left\{ -\frac{\frac{u^2}{\sigma_u^2} - \frac{2uv}{\sigma_u \sigma_v} + \frac{v^2}{\sigma_v^2}}{2(1 - \rho^2)} \right\} \ . \tag{9}$$

The input has effective bandwidths σ_u and σ_v for the u and v frequency coordinates respectively. After filtering the bandwidth is reduced to $\sigma_u/\sqrt{1 + \alpha}$ and $\sigma_v/\sqrt{1 + \alpha}$. For the case of $\alpha = 1$, the bandwidth is reduced by half in each dimension and the effective signal to noise ratio is squared.

2.1. ERS Tandem Mission example from the Jakobshavns Isbræ

Interferometric SAR data were collected over the glacier Jakobshavns Isbræ in North East Greenland by ERS-2 and ERS-1 on November 11 and November 12, 1995 and again 35 days later. ERS-1 and ERS-2 were in repeat orbit during the Tandem phase such that two co-registered interferograms could be produced from the 4 passes. The interferometric correlation of the glacier is shown in Figure 3. A combination of rapid motion and distortion of the glacier destroys correlation of the 1-day interferogram in the lower reaches of the glacier. Upstream, noisy fringes with correlation in the range of 0.2 to 0.5 are discernible. Regions with little motion or rock have high correlation $\gamma > 0.7$. For these data, 5 samples were averaged in azimuth such that the output sample spacing is approximately 20×20 meters.

Figure 3

The motion of the glacier can be derived from the two repeat-pass interferograms after unwrapping and does not require specific knowledge of the surface topography [Goldstein 1997; Gabriel, A. K. and R. M. Goldstein 1989]. The assumption must hold that motion of the glacier is constant during the two 1-day observation intervals. Alternately, only one pair is necessary if the baseline and surface topography are known. In this case a synthetic interferogram without phase related to the motion field can synthesized and subtracted from the observations [Rosen et al. 1996].

The standard deviation of the phase σ_ϕ is a meaningful measure of interferometric noise and can be estimated directly from the interferogram, both before and after filtering. Estimation of σ_ϕ requires removal of the local phase gradient $\bar{\phi}(i,j)$ over the estimation window,

$$\sigma_\phi = \left(\frac{\sum_N \left(\phi(i,j) - \bar{\phi}(i,j) \right)^2}{N-1} \right)^{\frac{1}{2}} , \qquad (10)$$

where N is the number of points in the rectangular estimation window. The edge width of the estimation window was 5 ($N = 25$) for estimation of both the correlation and phase standard deviation on the glacier.

Results from applying the filter ($\alpha = 1$) are shown in Figure 4. Also shown are maps of σ_ϕ for the unfiltered and filtered interferograms. Averaging over the first 32 lines of the segment, σ_ϕ improved from 0.68 to 0.19. Overall σ_ϕ of the interferogram segment improved from 0.78 to 0.33 radians. Since the filter is derived from the power spectrum, the filter has a broadband characteristic in noisy regions, but in areas where there are discernible fringes, bandpass filtering occurs. As α is increased, the threshold effect becomes more pronounced

Figure 4

compared to a low-pass filter with equivalent resolution.

Finally the interferograms were unwrapped using a residue based algorithm [Goldstein et al. 1988]. This step is necessary for quantitative analysis differential interferograms unless the total deformation is less than 2π in magnitude. Points of two-dimensional phase inconsistency determined by integration of the phase differences around closed paths are termed residues. Branch cuts between residues in the interferogram plane are used to restrict the phase integration path such that consistent values of the unwrapped phase are obtained. The number of residues in the unfiltered interferogram is 8551, and after filtering this is reduced to 1700. Large numbers of residues result in intersecting branch cuts that exclude phase unwrapping of some regions. Points were not unwrapped when σ_ϕ exceeded 1 radian. Using this algorithm, 92% of the filtered interferogram segment could be unwrapped, compared to 64% of the unfiltered segment.

3. Conclusions

The adaptive interferogram filtering algorithm significantly improves fringe visibility and reduces noise introduced by temporal or baseline related decorrelation The variable bandwidth of the filter, derived directly from the power spectrum of the fringes preferentially smoothes the phase in regions with high correlation, but remains broad-band in regions where the correlation is low. Radar interferograms have the property that the fringe spectrum is locally very narrow-band, except possibly in regions of radar layover where the phase is no longer single valued due to multiple scattering. These properties account for the success of the filter in suppressing noise.
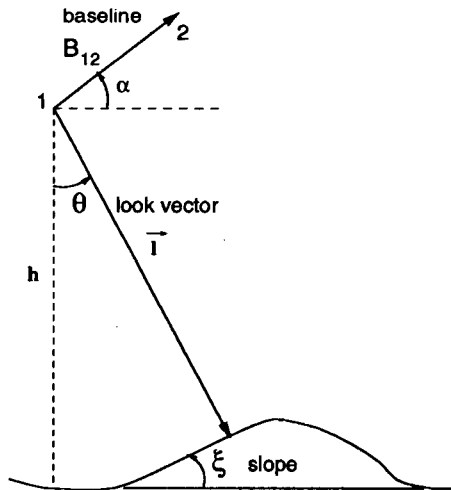
References

Li, F. K. and R. M. Goldstein, Studies of multi-baseline space-borne interferometric synthetic aperture radars, *IEEE Trans. Geoscience and Remote Sensing, 28,* 88-97, 1990.

Gabriel, A. K., Mapping Small Elevation changes over Large Areas: Differential Radar Interferometry, J. Geophys. Res., it 94, 9183-9191, 1989.

Goldstein, R. M., H. A. Zebker, and C. L. Werner, Satellite radar interferometry: Two-dimensional phase unwrapping, *Radio Science, 23,* 713-720, 1988.

Goldstein, R. M., H. Engelhardt, B. Kamb, and R. M. Frolich, Satellite radar interferometry for monitoring ice sheet motion: application to an Antarctic ice stream, *Science, 262,* 1525-1530, 1993.

Goldstein, R. M., Atmospheric limitations to repeat-track radar interferometry, Geophys. Res. Lett., *22,* 2517-2520, 1995.

Goldstein, R. M., and C. L. Werner, Radar Ice Motion Interferometry, 3rd *ERS ESA Symposium Proceedings, http://www.ers-symposium.org/data/goldstein,* 1997.

Joughin, I., R. Kwok, and M. Fahnestock, Estimation of ice sheet motion using satellite radar interferometry - method and error analysis with application to the Humboldt Glacier, Greenland, *J. Glaciology, 42,* 564-575, 1996.

Lee, Jong-Sen, K. Hoppel, S. Mango, and A. Miller, Intensity and Phase Statistics of Multilook Polarimetric and Interferometric SAR Imagery, *IEEE Trans. Geoscience and Remote Sensing, 32,* 1017-1027, 1992.

Massonnet, D., M. Rossi, C. Carmona, F. Adragna, G. Peltzer, K. Fiegl, and T. Rabaute, The displacement field of the Landers earthquake mapped by radar interferometry, *Nature, 364,* 138-142, 1993.

Peltzer, G. and P. A. Rosen, Surface displacement of the 17 May 1993 Eureka Valley, California, earthquake observed by SAR interferometry, *Science, 268,* 133-1336, 1995.

Rosen, P. A., S. Hensley, H. A. Zebker, F. H. Webb, and E. J. Fielding, Surface deformation and coherence measurements of Kilauea Volcano, Hawaii, from SIR-C radar interferometry, J. Geophys. Res., *101,* 23109-23125, 1996.

Zebker, H. A., S. N. Madsen, J. Martin, K. B. Wheeler, T. Miller, Y. Lou, G. Alberti, S. Vetrella, and A. Cucci, The TOPSAR interferometric radar topographic mapping instrument, *IEEE Trans. Geoscience and Remote Sensing, 30,* 933-940, 1992.

Zebker, H. A., and J. Villasenor, Decorrelation in interferometric radar echoes, *IEEE Trans. Geoscience and Remote Sensing, 30,* 950-959, 1992.

Zebker, H. A., C. L. Werner, P. A. Rosen, and S. Hensley, Accuracy of topographic maps derived from ERS-1 interferometric radar, *IEEE Trans. Geoscience and Remote Sensing, 32,* 823-836, 1994.
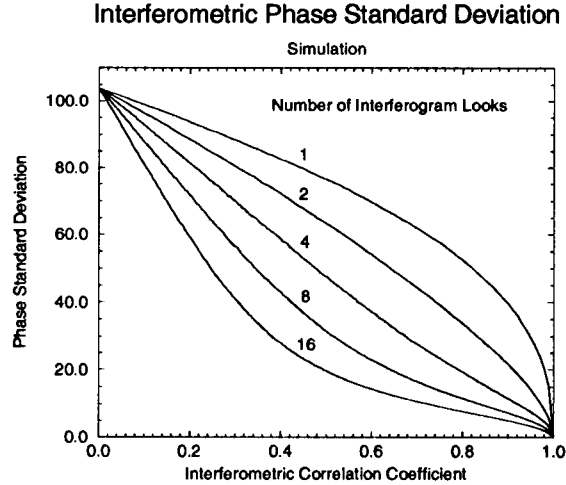
R. M. Goldstein and C. L. Werner, Jet Propulsion Laboratory, MS 300/227, 4800 Oak Grove Drive, Pasadena, CA 91109-8099. (e-mail: goldstein@kahuna.jpl.nasa.gov)

Figure 1. Interferometric imaging geometry. The vector between radar tracks is the baseline B rotated by the tilt angle α relative to a horizontal reference. The look vector $\vec{l}$ points from the radar to the imaged point on a slope defined by angle ξ.

Figure 1. Interferometric imaging geometry. The vector between radar tracks is the baseline B rotated by the tilt angle α relative to a horizontal reference. The look vector $\vec{l}$ points from the radar to the imaged point on a slope defined by angle ξ.


Figure 2. Phase noise standard deviation σ_ϕ as a function of decorrelation and the number of independent observations combined for each interferogram sample. interferogram.

Figure 2. Phase noise standard deviation σ_ϕ as a function of decorrelation and the number of independent observations combined for each interferogram sample. interferogram.
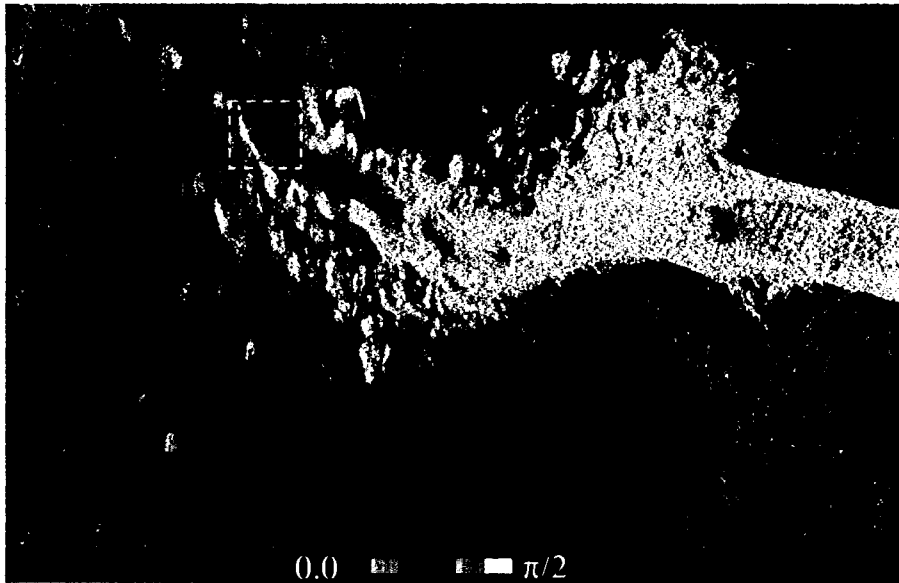
Figure 3. Phase standard deviation of ERS-1/ERS-2 Tandem interferogram of Jakobshavns Isbræ in North East Greenland (69°10′ N, 49°5′ W). The scene is approximately 68.6 x 43.5 km and is color coded for the local phase standard deviation σ_ϕ over the range $[0,\pi/2]$. Regions near the exit of the Glacier are completely decorrelated leading to a high σ_ϕ due to glacier motion over the 1-day interval. Intensity of the image is proportional to the radar brightness of the scene. The effects of filtering the interferogram in the marked rectangular region are shown in Figure 4.
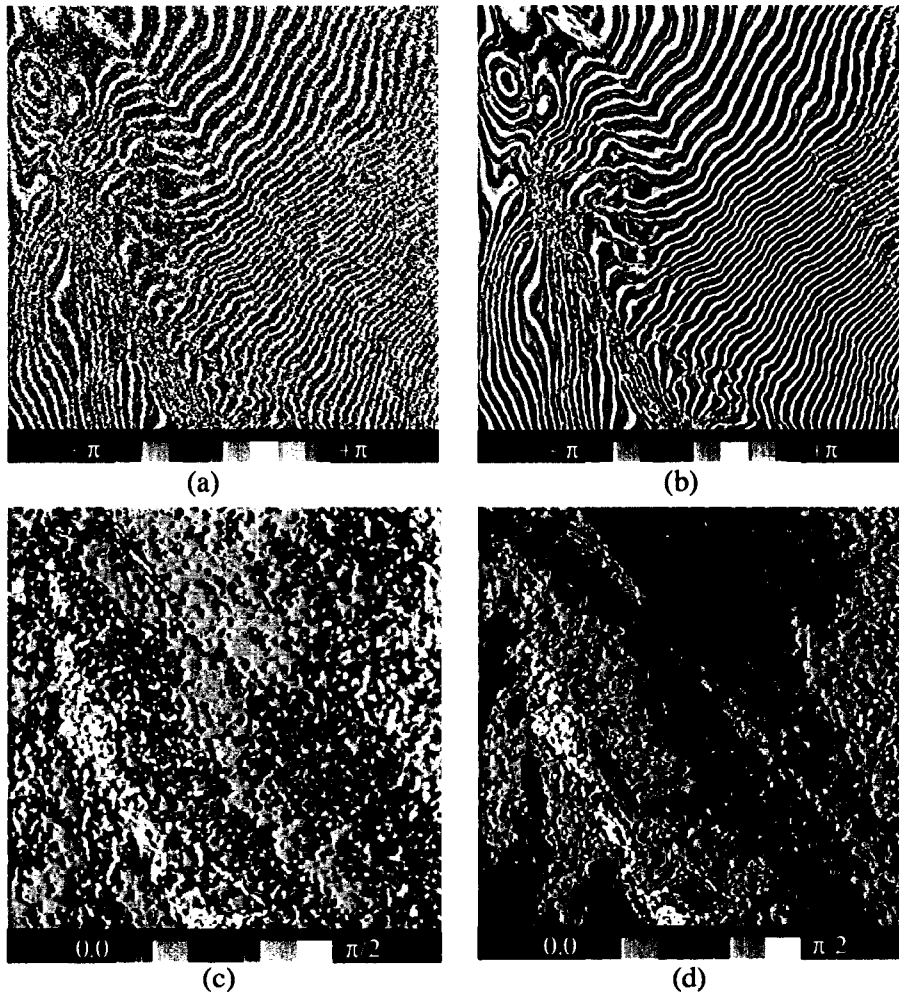
(a) (b)

(c) (d)

Figure 4. Comparison of unfiltered and filtered interferograms ($\alpha = 1$) of Jakobshavns Isbræ glacier. The standard deviation of the phase was evaluated using a 5 × 5 estimation window after subtraction of the local phase gradient. Resolution element size is approximately 20 × 20 meters. The interferogram phase is wrapped between $-\pi$ and $+\pi$. **(a)** Unfiltered 5-look interferogram phase; **(b)** filtered interferometric phase; **(c)** σ_ϕ for the unfiltered interferogram; **(d)** σ_ϕ after filtering.

Figure 4. Comparison of unfiltered and filtered interferograms ($\alpha = 1$) of Jakobshavns Isbræ glacier. The standard deviation of the phase was evaluated using a 5 × 5 estimation window after subtraction of the local phase gradient. Resolution element size is approximately 20 × 20 meters. The interferogram phase is wrapped between $-\pi$ and $+\pi$. **(a)** Unfiltered 5-look interferogram phase; **(b)** filtered interferometric phase; **(c)** σ_ϕ for the unfiltered interferogram; **(d)** σ_ϕ after filtering.

GOLDSTEIN AND WERNER: RADAR INTERFEROGRAM FILTERING